Case Studies in Construction Materials 20 (2024) e03359

Contents lists available at ScienceDirect

Case Studies in Construction Materials

journal homepage: www.elsevier.com/locate/cscm

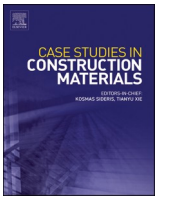

Comparative study on fracture evolution in steel fibre and bar reinforced concrete beams using acoustic emission and digital image correlation techniques

Shahzad Ashraf, Magdalena Rucka *

Department of Mechanics of Materials and Structures, Faculty of Civil and Environmental Engineering, Gdańsk University of Technology, Narutowicza 11/12, Gdańsk 80-233, Poland

ARTICLE INFO

Keywords:
Fracture monitoring
Steel fibre-reinforced concrete
Steel bar-reinforced concrete
Acoustic emission (AE)
Digital image correlation (DIC)

ABSTRACT

In recent decades, the demand for sustainable construction practices has increased, but raw materials such as reinforcing steel remain scarce. Therefore, steel fibres have emerged as a popular and sustainable choice in the construction industry, offering a cost-effective alternative to traditional steel bar reinforcement for both flatwork and elevated structures. The purpose of this study is therefore to compare the performance of fracture behaviour between steel fibre-reinforced concrete (SFRC) and steel bar-reinforced concrete (SBRC) beams subjected to three-point bending. The fracture process was monitored by using two non-invasive techniques: acoustic emission (AE) and digital image correlation (DIC). The damage level was identified by characterizing the parameter-based AE data such as hit rate, energy release, count, rise time, amplitude, and signal strength. DIC images were employed to visualise the crack propagation in parallel with the AE data. To further understand the fracture characteristics, the integration of 2D source localization of AE events (based on local AE fracture energies) with DIC results was investigated. The parameter-based AE results showed that SBRC beam experienced a high density of AE hits with large peak amplitude events that were accelerated during the pre-peak loading phase. The Ib-value analysis revealed that SBRC beam exhibited a higher degree of fracture magnitude during the primary crack development process than SFRC beam. Following the main cracking stage, SFRC beam demonstrated an improved post-cracking softening behavior and superior ability to arrest crack propagation compared to SBRC beam. The integration of local AE fracture energy and DIC results provided a novel approach for a better understanding of the fracture behaviour in both SFRC and SBRC beams. This study's findings contribute to more precise monitoring of fracture evolution in SFRC and SBRC beams, ultimately improving the selection process for primary reinforcement in flatwork and elevated structures.

1. Introduction

Concrete is the most widely consumed material in the world because of its remarkable and exceptional structural features like as durability, strength, cost-effectiveness, and flexibility [1,2]. However, it possesses significant disadvantages in terms of its limited ability to withstand high tensile load capacity and susceptibility to becoming brittle, leading to the formation of cracks in engineering

* Corresponding author.
E-mail address: magdalena.rucka@pg.edu.pl (M. Rucka).

https://doi.org/10.1016/j.cscm.2024.e03359
Received 3 February 2024; Received in revised form 21 May 2024; Accepted 28 May 2024
Available online 29 May 2024

applications [3]. Because of these constraints, conventional concrete cannot be used to construct complex and unique structures, like concrete bridge decks and slabs subjected to mechanical loading [4], offshore structures [5], or prefabricated reinforced concrete frameworks [6]. To address these issues, steel reinforcement is used in the tensile region of the structures to enhance their durability and strength. It provides support to operate as a single unit to ensure a cohesive relationship between the concrete and steel rebar under static and dynamic loads [7,8]. Although steel reinforcements have been extensively utilized, because of their high reinforcement ratio, they are still posing numerous demerits to prevent reinforced concrete (RC) structures from exhibiting tensile and flexural cracks. To address this issue, discrete steel fibres are added to concrete to increase ultimate strain, fatigue resistance, tensile strength, and flexural capacity while minimizing fracture width and requiring thickness, thus leading to the modified concrete being termed steel fibre-reinforced concrete (SFRC) [9]. SFRC possesses a higher modulus of elasticity as compared to ordinary concrete, making it highly suitable for reinforcing applications as well as limiting the extent of cracks propagation into macroscopic scale. It offers practical solutions for several engineering problems, such as enhancing crack resistance in long-span suspension bridges, addressing concerns like shrinkage cracking, and improving highway structural durability [10]. However, there is an emerging trend in the construction industry where manufacturers are offering an innovative approach to replacing steel reinforcement with steel fibres in concrete pavements and floors as a sustainable, cost effective and practical solution to traditional practices. Therefore, it is essential for both researchers and designers to have a thorough understanding of the fracture behaviour of steel fibres compared to steel reinforcement when selecting materials for primary reinforcement [11]. In this regard, several non-destructive (ND) and elastic wave evaluations have been extensively employed to identify fracture process mechanisms and monitor their development in concrete elements reinforced with fibres and steel rebar. Among those NDT evaluations, acoustic emission (AE) [12] and digital image correlation (DIC) [13] have shown excellent outcomes in evaluating the internal imaging of concrete fractures over time. The combined AE and DIC methods are highly sensitive for the determination of early-stage damage and their ability to pinpoint the source of the damage. Their ability to monitor fracture development in real time allows for the early detection and evaluation of damage when structures are loaded, enhancing the structural integrity and safety of RC structures throughout their service lives. Both techniques have been effectively employed by numerous researchers in concrete structures to examine fracture evolution and deformation characteristics, and have provided a thorough review of failure mechanisms. To validate the AE technique, Gallego et al. [14] studied the bonding behavior of black and hot-dip galvanized deformed bars of concrete specimens exposed to pull-out tests. They examined the AE activities and discovered varied patterns of the various bond degradation phases among the steel types used. Similarly, the AE technique performed by Abouhussien and Hassan [15] in reinforced concrete structures to assess the bond integrity between steel to concrete matrix interface through pull-out tests. The results showed that there is strong correlation between different stages of bond damage mechanism and AE characteristics parameters. Saliba and Mezhoud [8] utilized the AE technique in parallel with DIC methods in reinforced concrete (RC) to analyse the influence of bar diameter on steel-concrete bond strength and their fracture properties using pull-out and tensile tests. It has been found that the applied force intensity was correlated with the activity of AE parameters and various stages of fracture observed at the steel-concrete interface. Further, the AE approach allows for assessing the effectiveness of bar reinforcing and the degree of damage in reinforced concrete and cement composites, as demonstrated by Tsangouri and Aggelis [16]. Apart from concrete and composite structures, Chai et al. [17] investigated the AE data and reported efficient monitoring for the progression of fatigue damage in stainless steel. In addition, AE data can be used to predict the size of fractures in stainless steel when subjected to varying load ratios.

Also, it's worth mentioning, that the AE approach could be further optimized for a specific type of damage monitoring of structures through advanced clustering and algorithmic functions to categorize the AE signals acquired through the failure and damage processes of concrete elements. Several recent studies have put forward and validated these advanced approaches to identify several damage progressions like cracking in cementitious composites, delamination, fibre pull-out, and debonding between steel/concrete-matrix interface through AE events (e.g. [18,19,20]). For example, Saha and Sagar [21] employed the K-means ++ clustering on the AE waveform features based on wavelet packet decomposition (WPD) to categorize fibre pull-out and cementitious cracking in SFRC. Similarly, Tayfur et al. [18] used the centroid-based clustering algorithm (K-mean) to examine AE parameters which successfully clustered the matrix cracking and steel fibre/matrix debonding damage mechanism of SFRC. In the field of civil engineering, many studies on reinforced concrete structures such as bridges and buildings have used 1D,2D, and 3D AE source localization techniques to increase the sensitivity of structural damage detection and the accuracy of crack localization (e.g. [22–27]). Compared to more sophisticated analytical methods, the monitoring technique using sensors and data acquisition units has become quite feasible for the AE localization of crack sources in concrete structures. De Smedt et al. [28] studied investigated AE source localization to evaluate damage development phases and fibre placement in SFRC using an AE damage-based monitoring technique. Their findings demonstrated that as the crack widened, AE events became more concentrated in the vicinity of the remaining active fibres. Bakour et al. [29] interpolated the 2D localization of AE events in terms of local fracture energy to examine FPZ development in larger concrete specimens using combined AE/DIC techniques. Their findings showed that local AE energy events were found to be more scattered and occurred at a greater distance from the main splitting macrocrack, while events with higher energy followed the path of the splitting macrocrack. Boniface et al. [30] studied the 3D AE source localization accuracy in concrete for accurate monitoring of crack localization and detection by using different algorithms. The results show that higher activity of AE events was detected around the damaged area, and AE-detected results are validated with DIC images. Also, in the work of Okeil et al. [31] DIC technique was employed to investigate local bond behavior and fracture mechanism around the reinforcing bars within a concrete/cement paste. The DIC results show there are large variations of crack propagation were observed within the cement paste and concrete specimen which originated from the steel bar surface. Xing et al. [32] studied the DIC technique to examine crack propagation in steel fibre-reinforced carbon nanotube (SFs-CNT) concrete under various flexural loading conditions. The results obtained from DIC images indicate that hybrid SFs-CNTs specimens demonstrated superior ductility behavior owing to SF's abilities to prevent fracture propagation and reduce the degree

of damage. In the recent past, some very analogous efforts have been provided in the scientific community, where AE, DIC, and dynamic identification were applied together, to investigate fracture process mechanism in plain concrete beams [33].

As the demand for more sustainable construction grows and raw material shortages like steel continue to be a challenge, steel fibres have become an increasingly popular choice in concrete pavements, flooring, and elevated structures due to their higher absolute strength, excellent fracture toughness, better crack width control, and good cost-effectiveness. The replacement of steel reinforcement with steel fibres in flatwork and elevated structures makes our built environment more sustainable, resilient, and efficient. However, there is a scant analysis that explores the real-time monitoring of the fracture behaviour of SBRC and SFRC beams in comparative terms for selecting concrete structures as primary reinforcement. To fill this information gap, the current study conducted an experimental investigation on fracture evolution between SFRC and SBRC beams using non-invasive methods. A three-point loading arrangement was used for conducted bending on concrete beams reinforced with steel fibre 0.6% by total vol. and a reinforcing bar diameter of 6 mm. The non-invasive inspection was done by taken AE signals and DIC images of the damaged samples at the same time underwent bending tests. Several statistical methods were used to analyse the AE signals, including the cumulative number of hits, peak amplitude distribution, cumulative energy analysis, Ib-value method, intensity analysis, and *k*-means clustering algorithm, to compare the fracture behaviour of SBRC and SFRC beams. The DIC method was used in parallel with the AE method to monitor the surface crack localization and validate the fracture evolution results of AE data. To validate the fracture evolution results of both AE and DIC testing data, the correlation between 2D source localization of AE events in terms of local fracture energy was also studied.

2. Materials and methods

2.1. Mixtures and specimens

Two concrete mixes, both based on the same design, were produced in the test programme. Mixture #1 was the plain concrete (PC), consisting of cement CEM I 42.5 R (380 kg/m^3), water (165 kg/m^3), aggregate 0/2 mm (648 kg/m^3), aggregate 2/8 mm (426 kg/m^3), aggregate 8/16 mm (754 kg/m^3) and superplasticizer (0.8% of the cement content). Mixture #2 was similar to mixture #1 but also contained steel fibres (SF) at a rate of 0.6% of the total concrete volume. The steel fibres were 25 mm in length, 0.5 mm in diameter, and had hooked ends. In addition, a 6 mm diameter steel bar was used as a reinforcement to produce a reinforced concrete sample based on mixture #1. The steel reinforcement used in this study is shown in Fig. 1a.

Three 10 × 10 × 50 cm^3 concrete prisms were prepared. The first was made from mixture #1, the second from mixture #2 and the third from mixture #1 with the steel bar embedded in it. After that, beam specimens of 4 × 4 × 16 cm^3 were then cut from the prisms. The beam specimens were cut from the inside of the prisms, i.e., none of the walls of the beams coincided with the walls of the prisms. The specimens used for the experimental analysis were as follows: a plain concrete (PC) beam, a steel-fibre reinforced concrete (SFRC) beam, and a steel bar reinforced concrete (SBRC) beam. Three samples from each group of mixtures were tested. All samples from each group showed similar behaviour and therefore, for clarity of the paper, only one from each group was selected for presentation. Side views on the beam tested with the position of the rebar are presented in Fig. 1b. Fig. 2 depicts a flow chart diagram illustrating of methodology and testing procedure conducted in this study.

2.2. Experimental setup and procedure

The experiment was conducted using a Zwick/Roell Z10 universal testing machine (UTM) setup equipped with a 10 kN load cell. The tested beams were subjected to three-point bending loading with two steel supports placed 120 mm apart, as shown in Fig. 3a. Firstly, beams were subjected to a preload of 50 N initially at a constant speed of 0.1 mm/min.

During the bending process, fracture behaviour was monitored using two non-destructive methods, including acoustic emission (AE) and digital image correlation (DIC). To record the AE signals, four Noliac NAC2024 multilayer piezoelectric AE sensors were attached to the front of the beam, as shown in Fig. 3b. Their resonant frequency is higher than 500 kHz, according to the manufacturer's specifications. Due to their small size (3x3x2 mm^3), such PZT sensors are particularly suitable for AE monitoring of small samples with limited mounting space. The data acquisition was carried out using the AMSY-6 system (Vallen Systeme GmbH) with a sampling rate 10 MHz and a threshold value set at 34 dB. The DIC measurement was conducted using the ARAMIS 3D Professional software system, and a time step of 1 s was taken.

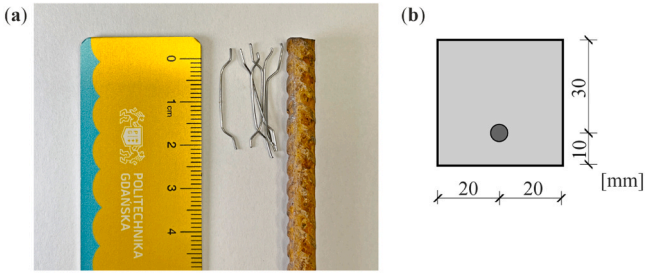

Fig. 1. Photograph of steel fibres and steel bar used in the study (a) and the beam cross-section with the position of the reinforcing bar.

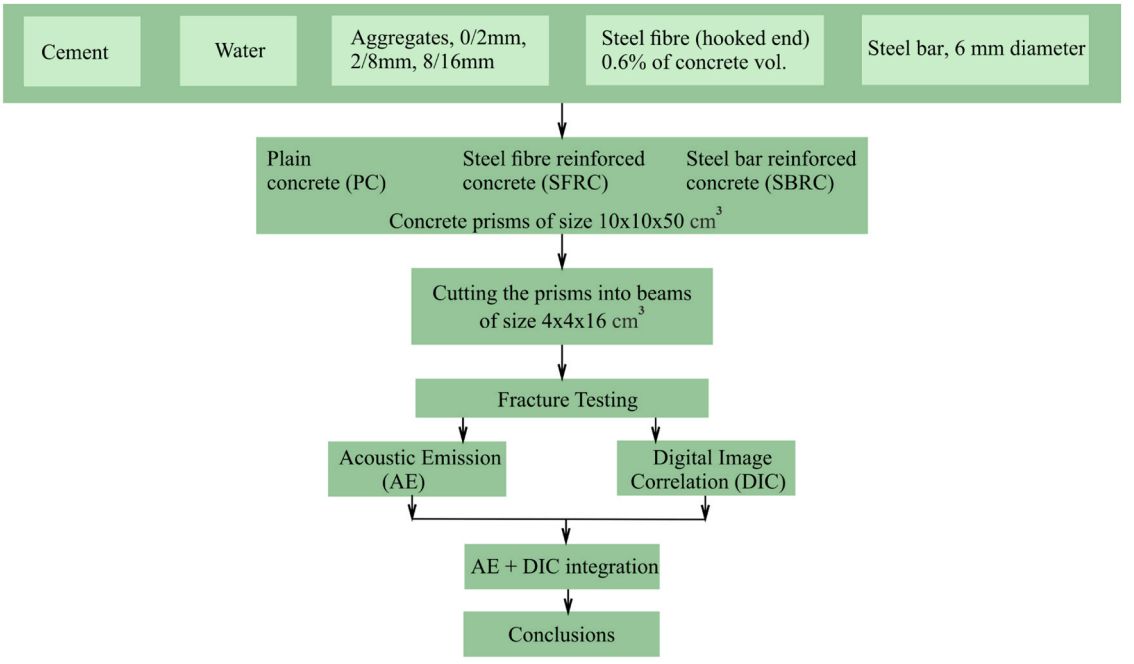

Fig. 2. Flowchart of the methodology and testing Process.

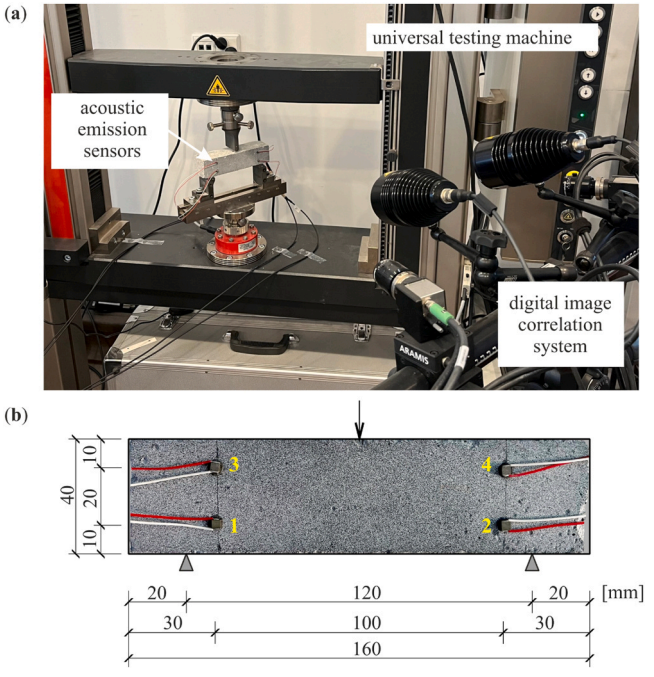

Fig. 3. (a) Experimental setup for AE and DIC; (b) and the concrete beam subjected to 3-point bending with the location of AE sensors (no. 1–4).

2.3. Acoustic emission

Acoustic emission (AE), one of the NDT techniques, allows real-time monitoring and detection of micro- and macrocracks in reinforced concrete structures. In this section, the fracture behavior of SFRC and SBRC beams was analyzed using the AE characteristics distribution parameters, such as the cumulative number of AE hits, AE peak amplitude distribution, cumulative absolute energy analysis, an Ib-value method, signal intensity analyses, and the K-Means clustering algorithm.

2.3.1. Ib-value method

T. Shiotani et al. [34] proposed the Ib-value approach by adding statistical values from the amplitude distribution of AE events. In Ib-value analysis, the amplitude range is established by calculating the mean value (μ), standard deviation (σ), higher($\alpha_1\sigma$) and lower amplitudes ($\alpha_2\sigma$), calculated as follows:

$$Ib = \frac{\log_{10}N(\mu - \alpha_1\sigma) - \log_{10}N(\mu + \alpha_2\sigma)}{(\alpha_1 + \alpha_2)\sigma} \tag{1}$$

where α_1 and α_2 are the user-defined constants related to the materials, ranging from -1 to 1. $N(\mu - \alpha_1\sigma)$ is the number of AE events with amplitudes greater than $\mu - \alpha_1\sigma$, and $N(\mu + \alpha_1\sigma)$ is the number of AE events with amplitudes greater than $\mu + \alpha_1\sigma$. The Ib-value exhibits quite sensitivity to minor damage events, hence the statistical value is usually set to the nearest 100 hits (N=100) [35].

2.3.2. AE signal intensity

This statistical approach is usually used to determine the level of deterioration and integrity of an RC structure, and is typically performed using the two parameters; historic index (*HI*) and log severity index ($\log_{10}(S_r)$)[36]. Both HI and lg S_r indices are calculated based on AE signal strength which takes the amplitude and duration into account. *HI* is defined as the real-time change in cumulative signal strength of the most recent AE events throughout the fracturing process [37]. The HI value is independent of structural size, as new damage can be monitored based on the HI value. The severity index (S_r) is defined as the average of 50 AE signal intensity with the largest peak amplitude value of signal intensity [37]. The two indexes are computed as follows:

$$HI(t) = \frac{N}{N-K}\frac{\sum_{i=K+1}^{N} S_{oi}}{\sum_{i=1}^{N} S_{oi}} \tag{2}$$

where $HI(t)$ is the historic index at time t, N is the number of hits up to time t; S_{oi} is the signal strength of the i^{th} hit, and K is the empirical constant based on the number of AE signals collected and material type;

$$S_r = \frac{1}{J}\sum_{i=1}^{J} S_{oi} \tag{3}$$

where S_{oi} is the i^{th} largest signal strength, and J represents the empirical parameter related to the type of materials monitored. The K and J values related to concrete materials are given in Table 1.

2.3.3. Data clustering using k-means clustering

K-means clustering is a widespread and powerful unsupervised algorithm known for its simplicity and computational efficiency. It works by initially setting specific centroids according to a given number of clusters (k). In the second step, each data point is then assigned to the cluster with the closest centroid based on the distance calculation. Lastly, the algorithm iteratively calculates the average distance between the data points within each cluster to update the centroids until optimal positions are reached, ensuring that all data points are correctly assigned to their respective clusters [38].

2.4. Digital image correlation

The DIC technique was used during the fracturing process of specimens to measure the strain field intensity and identify the locations of damaged zones. A rectangular area of interest of 100 × 40 mm^2, located on the surface of the beam was selected for non-contact inspection. This region was divided into 19 × 19 pixels with 10 pixels distance. Subsequent images were compared to a reference image taken in the intact (reference) state, allowing the recording of changes in pixel group motion and the calculation of displacements/deformations. This enabled the observation of the development of strain and crack formation characteristics.

3. Results and discussion

3.1. Bending test results

Fig. 4 shows the different failure modes of tested beams that underwent bending processes. For the SBRC beam (as shown in Fig. 4c), surface cracks generated on the front face of the beam due to a splitting concrete failure phenomenon occur at the steel-

Table 1
K-parameter and J-values.

No. of hits (N)	≤50	51–200	201–500	≥501
K	0	N−30	0.85 N	N−75
J	0	50		

concrete interface. This indicates that tensile forces exceed the shear capacity of the concrete, resulting in wider longitudinal cracks extending to the outer surface. Meanwhile, the incorporation of steel fibres into the ordinary concrete refrains the formation of initial cracks within the matrix, resulting in shorter crack length propagation compared to the SBRC beam (as shown in Fig. 4b). This shows that the presence of steel fibres inhibits the crack growth zone and reduces the degree of damage to concrete.

The load-deflection curves of PC, SFRC, and SBRC beams are presented in Fig. 5. It was observed that all tested beams exhibited a similar trend of load-deflection profile after attaining peak load-carrying capacity; sudden brittle failures were observed. The maximum load values registered for PC, SFRC, and SBRC beams were 3283.80 N, 4461.72 N, and 9331.0 N, respectively. The time of maximum bending force for the PC, SFRC, and SBRC beam was 183 s, 255 s, and 648 s, respectively. The introduction of steel fibres and steel bar reinforcement to ordinary concrete resulted in a higher bending capacity. The load-deflection curve of the SFRC beam showed a progressive decrease in load after the major fracture developed, indicating that it can withstand load even after the main crack. The reason for reducing the incidence of cracks is that the steel fibres operate as micro reinforcements, which are consistently distributed throughout the matrix, bridging the gap in the fractured area, and thus reducing fracture development. The crack-arresting mechanism was observed in the load-deflection curve, which remained flat until the peak load. On the other hand, the load-carrying ability of SBRC beam decreases dramatically once the main fracture has developed. This is because SBRC beam rely solely on the steel rebars to provide tensile strength. In the absence of fibers, cracks can spread more rapidly, leading to a steeper decline in load.

3.2. Acoustic emission results

3.2.1. Cumulative hits distribution

The cumulative AE hit activity has been widely employed in materials engineering for damage characterizations inside materials. The cumulative number of hits activity is highly correlated with the damage initiation and propagation inside the concrete [39,40]. Fig. 6 illustrates the cumulative AE hit activity profile along with load curves of PC, SFRC, and SBRC beams during the fracturing process. The cracking pattern is divided into three distinct phases, taking into account the changes in the slope of the cumulative hit curve, according to [8]. These phases were identified as the pre-peak (I), peak (II), and post-peak (III).

For the normal concrete beams, it can be observed that a low-intensity AE activity was recorded during the pre-peak phase. The density of the AE hits increases rapidly with the loading increases, indicating the transformation of microcracks into macrocracks inside the concrete. During the post-cracking failure stage (II), the slope of the accumulated AE hit rate gradually decreased until the specimen collapsed. However, the incorporation of steel fibres and bar reinforcement significantly modified the structural properties of concrete. For SFRC beam, a low hit AE rate with a stable profile was observed during the pre-peak phase I. This is due to fact that to the bridging effect of steel fibres with the cement matrix, which improved the workability of the resultant matrix and inhibited microcrack propagation. However, during the peak phase (II), there was a noticeable increase in cumulative hit rate, suggesting the micro-cracks coalesced and rapidly developed into macrocracks. In the post-peak phase (III), SFRC beam showed a higher number of AE signals with a longer duration as compared to previous stages. This can be attributed to the fibres entering the traction-free zone and continuously redistributed stresses making a significant contribution to the crack resistance. As a result, a greater number of AE signals were generated.

In the case of the SBRC beam, it was found that a few AE hit activities were observed during the pre-peak phase (I), indicating perfect bonding between the steel and concrete matrix interface. As the load continues to increase (phase II), the cumulative hit curve is significantly accelerated, indicating the nucleation of microcracks along the weakest planes of bar reinforcement. As a result, a

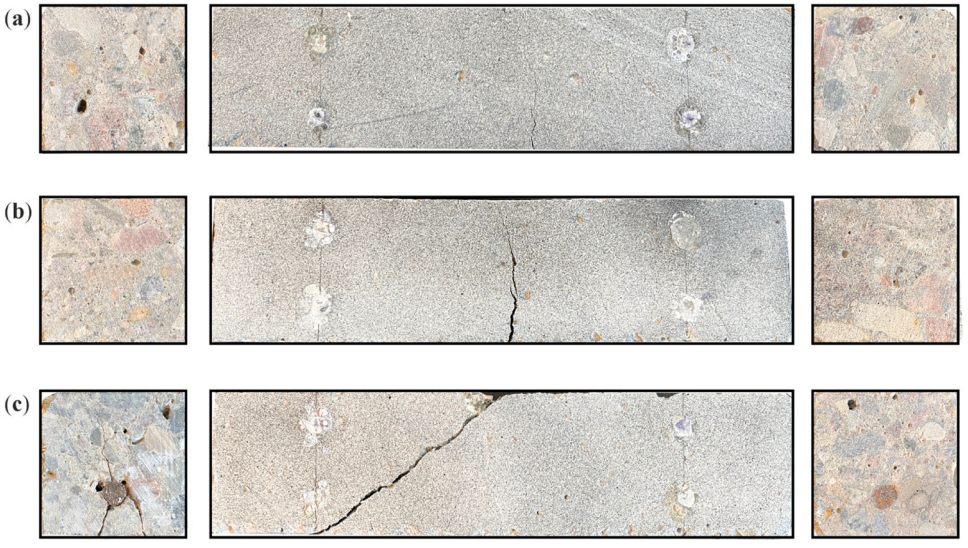

Fig. 4. Failure patterns of tested beams after the bending process: (a) PC; (b) SFRC; and (c) SBRC.

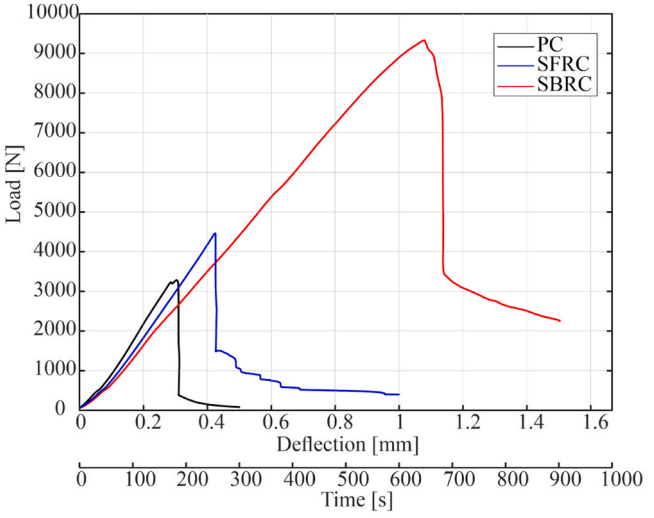

Fig. 5. Load-time curves of PC, SFRC, and SBRC beams.

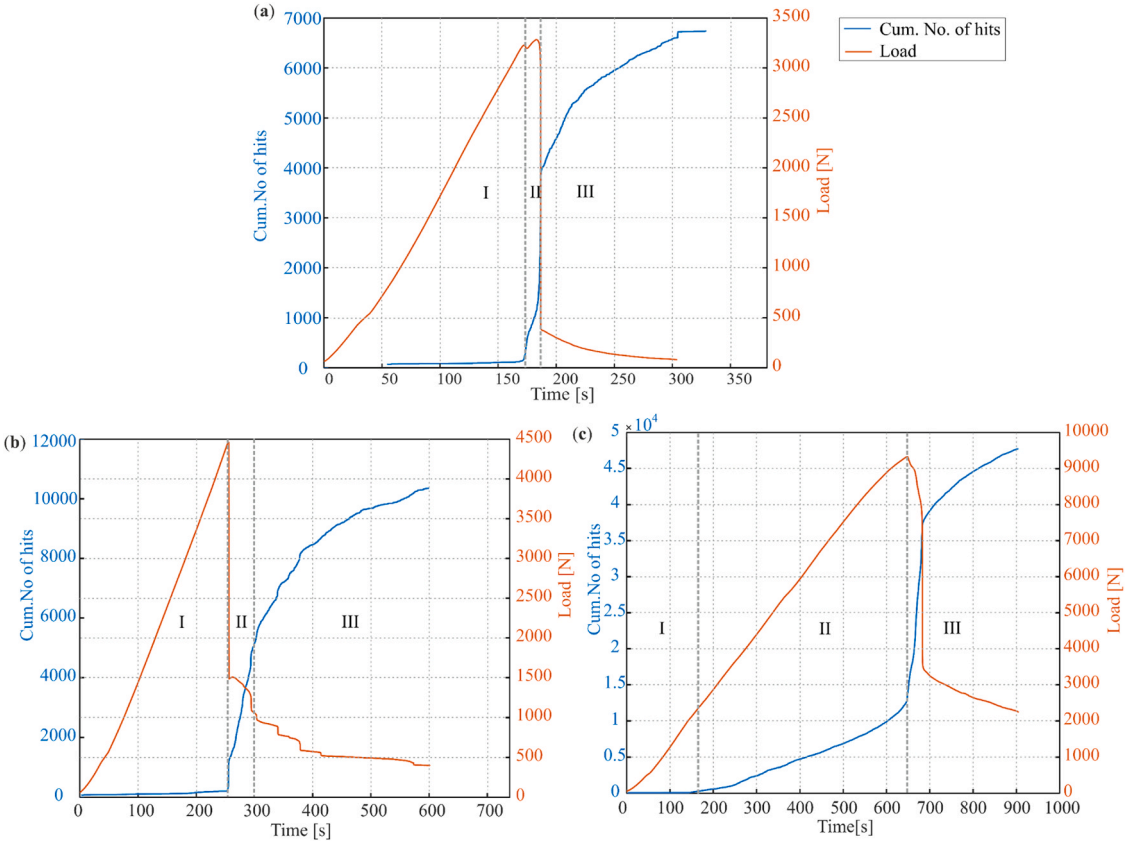

Fig. 6. Cumulative number of AE hits with load-time curve: (a) PC; (b) SFRC; and (c) SBRC.

higher level of microcracking activity was observed in SBRC beam as compared to SFRC beam. The intensity of AE hit activity increased rapidly in phase III, which was characterized by a noticeable and rapid increase in the AE hit profile. Those higher hits are attributed to brittle failure due to the occurrence of multiple splitting concrete failures and insufficient cover thickness with emissions of higher AE activity as compared to SFRC beam. A comparison of AE hit fracturing results showed that the SFRC beam sustained the post-peak (III) loading phase for a more extended period, signifying its ability to curtail crack propagation and produce less degree of damage to concrete.

3.2.2. Peak amplitude events distribution

The amplitude distribution is an important parameter of the AE waveform to describe the damage level and instability of the RC failure [41]. Fig. 7 depicts the fracture evolution of PC, SFRC, and SBRC beams during the bending process. It can be observed that the peak amplitude events of tested beams increase accordingly as the loading rate increases. This indicates that the microcracks nucleate and increase gradually during the initial fracturing process. As the loading rate increases, microcracks rapidly coalesce into macro-cracks. Finally, macrocracks expand rapidly, resulting in macroscopic damage characterized by higher amplitude events. According to Sagar et.al [42], AE events with amplitudes reaching from 45 to 70 dB are indicative of minor damage, while amplitudes in the range of 71–90 dB suggest moderate damage. In addition, AE events ranging from 91 dB to 100 dB are associated with major damage.

In Fig. 7, it is noticeable that the SFRC beam exhibited a relatively low damage zone during the pre-peak loading phase, and low peak amplitude events ranging from 35 dB to 60 dB were observed. This indicates that the crack-bridging ability of the steel fibres leads to shrinkage of the microcracks at the interface between the fibres and the cement matrix, resulting in limited crack propagation in the matrix. However, notably higher peak amplitude events were observed during the peak and post-peak phases. The peak amplitude events reached up to 93 dB in the peak failure phase and ranged from 35 dB to 70 dB in the post-peak failure phase. The main reason for this phenomenon is that at the peak loading period, fibre debonding behaviour was generated, causing rapid nucleation of macrocracks. After the peak phase, the crack width increases as fibres enter the tensile-free zone and continuously redistribute stresses, which contribute significantly to the crack resistance.

For the SBRC beam, higher peak amplitudes were observed during the peak (II) and post-peak phases (III), indicating that a higher degree of microcracking activities was observed in the SBRC beams compared to the SFRC beam. During the initial phase, low peak amplitude events were recorded at 43 dB, signifying a strong bond adhesion strength between the bar reinforcement and the concrete elements. As the load level gradually increased, higher peak amplitude events ranging from 35 dB to 82 dB were detected. These higher amplitude events signified the initiation of multiple microcracks originating from the bar reinforcement and their subsequent propagation in the radial direction. This indicates that the SBRC beam showed gradual crack development during the pre-peak phases and the concentrated damage localization area continued to increase until the stage of peak load was reached. When the load reached its maximum point, a brittle rupture was observed due to the splitting of the concrete. At this point, higher amplitudes of 90 dB were observed. After the main cracking stage, higher amplitude events up to 90 were recorded. This indicates that the lack of distributed fibres did not significantly enhance the ductility of the beams after the onset of main cracking failure.

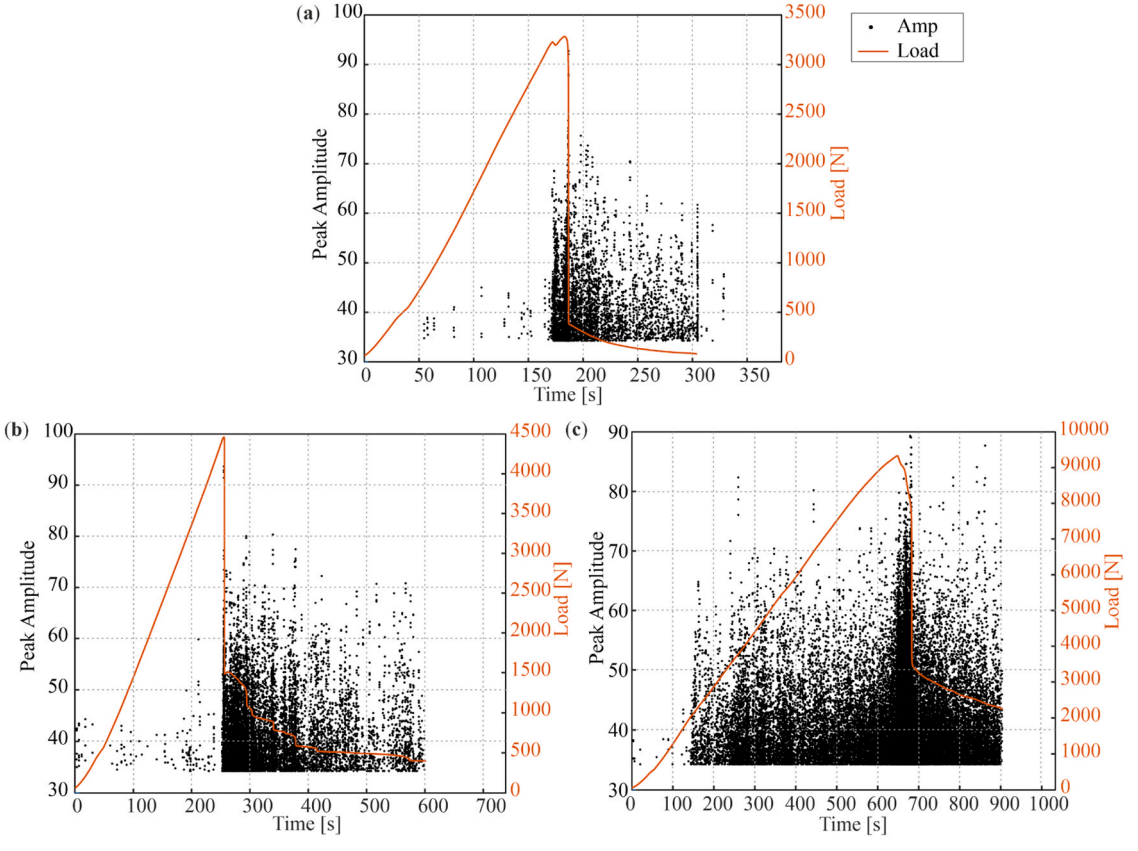

Fig. 7. The distribution of peak amplitude events together with load-time curve: (a) PC; (b) SFRC; and (c) SBRC.

3.2.3. Cumulative AE energy analysis

The emitted energy of AE events during microcrack propagations is estimated by evaluating the AE data with statistics analysis and fracture theories [43]. According to recent research [44,45], the total energy (R) released during damage processing in quasi-brittle materials is represented by the summation of dissipated energy (D) and emitted energy (E) at the snap-back point. The relationship between AE absolute energy rate and damage evolution is particularly useful for detecting and monitoring crack growth size and concrete's structural integrity [46]. Fig. 8 illustrates the cumulative energy hit profile together with the load-time curve of PC, SFRC, and SBRC beams. During the pre-peak phase, the stable AE energy hit profile in the SBRC beam was observed. This indicates a strong bond exists between the bar reinforcement and the concrete, which contains higher strain energy, and the testing machine requires more force for failure. As the load increased, the SBRC beam exhibited a variation in the slope of the energy hit profile until it reached the maximum loading stage. This nonlinearity behaviour was ascribed to the direct correlation between the slippage of the bar reinforcement and the formation of splitting cracks in the concrete matrix itself. This phenomenon leads to the emission of high-energy AE signals with greater damage and higher intensity. At the peak phase, these smaller microcracks coalesced and developed into marco-cracks, which led to the failure of the specimen.

For the SFRC beam, the cumulative energy hit profile has a distinctly flat section up to the peak load stage. This indicates that the presence of the steel fibres creates multiple paths and efficiently acts as a bridge over the fracture areas, so impeding their fast propagation of microcracks. This crack-bridging effect increases the ductility of the material by enabling it to absorb energy through non-elastic deformations. At the peak loading phase, an abrupt increase in the AE energy profile in SFRC beam was observed due to a fibre debonding behaviour caused by rapid nucleation of macrocracks at the weaker cracked surface area. However, after the main cracking phase, the SFRC beam maintain load-carrying capacity and absorb more energy than SBRC beam. When the fibers entered the traction-free zone, they did not contribute significantly to fracture resistance until the beam failed.

3.2.4. Ib-value analysis

The variations in Ib-values provide valuable insights into fracture mechanisms related to micro- and macrocracks in the reinforced concrete material. The increasing trend of the Ib-value indicates microscopic fractures, which tend to produce more AE hits with lower amplitudes. Conversely, a decreasing trend of Ib values resulted in fewer AE hits with higher amplitudes, indicating macroscopic fractures [12,47]. Fig. 9 exhibits the Ib values variations of PC, SFRC, and SBRC beams with group sizes of ($N = 100$) along with the load-time curve. It can be observed that the Ib-value for the SFRC beam demonstrated a higher value during the initial fracture process indicating that a lower number of microcracks had initiated until the load approached the maximum value. This can be attributed to the crack-bridging capacity of the steel fibres which shrink the microcracks at the interface between fibres and the cement matrix,

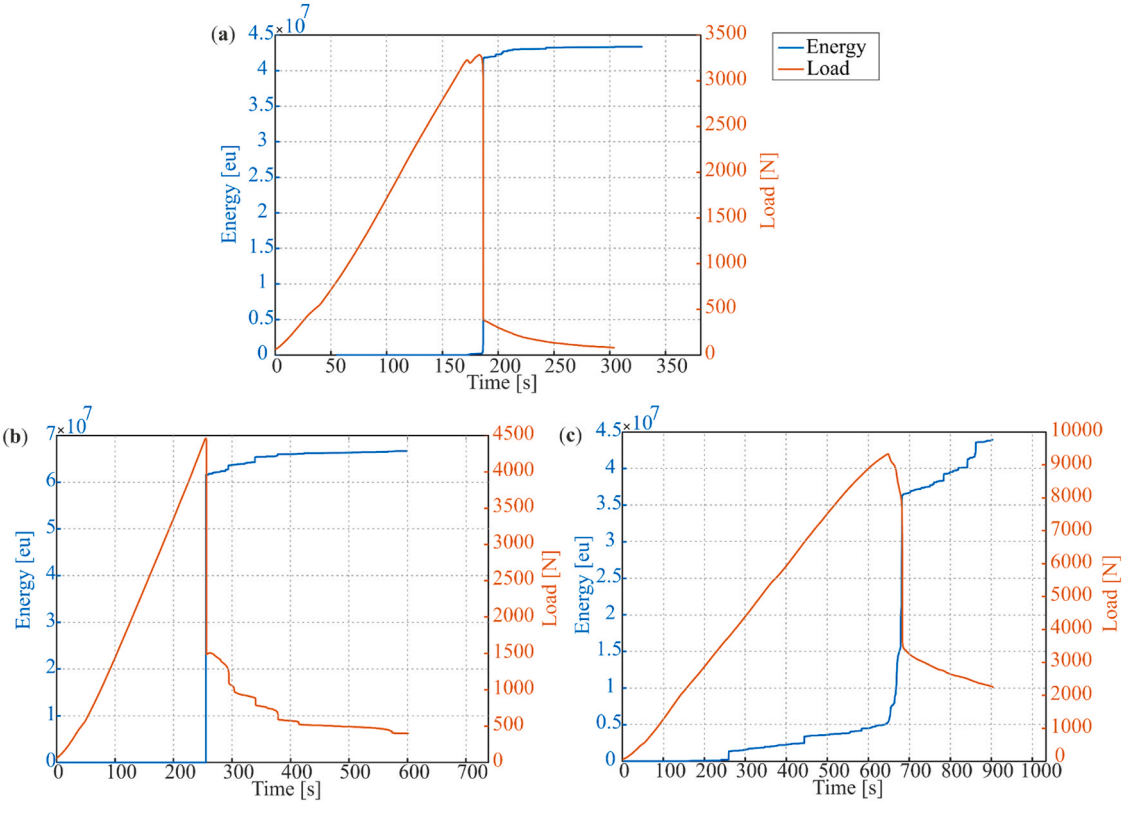

Fig. 8. Cumulative AE energy profile together with load-time curve: (a) PC; (b) SFRC; and (c) SBRC.

resulting in a limited extent of crack propagation within the matrix. However, the Ib-value profile experienced a sudden decrease at the peak loading stage, indicating fibre debonding behaviour causing rapid nucleation of macrocracks. After the peak loading stage, the Ib-value experienced substantial fluctuations due to the continuous reinforcement provided by the steel fibres, and finally the specimen collapsed due to the complete pull-out of fibres from the cracked-bridged area.

On the other hand, the SBRC beam experienced continuous variations in the Ib value, with a relatively higher AE amplitude recorded during the initial fracture process. This suggests that there was an increased occurrence of microcracking activities along the radial direction of the bar reinforcement, and the number of microcracks was larger compared to the number observed in the SFRC beam. As the loading time increased, the Ib value pattern exhibited a descending trend. This indicates that the SBRC beam showed gradual crack development phases and the concentrated damage localization area continued to increase until the stage of peak load was reached. At the peak loading stage, a lower Ib-value was observed as compared to the SFRC beam, due to interconnected microcracks causing larger crack widths and eventual macroscopic damage to the beams. After the primary cracking phase, the interface between the steel reinforcing bar and the matrix did not play a significant role in increasing the ductility. As a result, the ability to transfer loads at the steel-matrix interface was reduced. Consequently, the SBRC beam tend to have a higher degree of brittle failure compared to the SFRC beam. A comparison of Ib-values at the major cracking stage between SFRC and SBRC beams found that the SBRC beam had a lower Ib value of 0.029 and generated macroscopic damage than the SFRC beam, which had a value of 0.039. This indicates that the fracture magnitude during the formation process of the primary crack in the SBRC beam is larger compared to the SFRC beam.

3.2.5. *AE signal intensity*

Fig. 10 presents the damage variation values of PC, SFRC, and SBRC beams based on two indices: the historic index HI(t) and the log severity index log10 (Sr). The HI(t) curves exhibited several local peaks, with each peak coinciding with a sharp rise in the log10 (Sr) curve, indicating the formation of some new cracks [46]. As can be noticed, the HI(t) value of the normal concrete beam displayed a single peak, which coincides with the occurrence of the major crack formation (183 s). For the SBRC beam, exhibited continuous variations during the entire fracture process and had consistently higher values than normal and steel fibre reinforced concrete. This indicates accelerated AE activities and ongoing damage processes in the SBRC beam throughout the fracture process. During the preliminary fracturing phase, a low profile of HI(t) was observed, along with continuous AE activity up to the peak loading phase. This phenomenon demonstrates that sliding of the bar reinforcement have generated the initiation of numerous microcracks within the

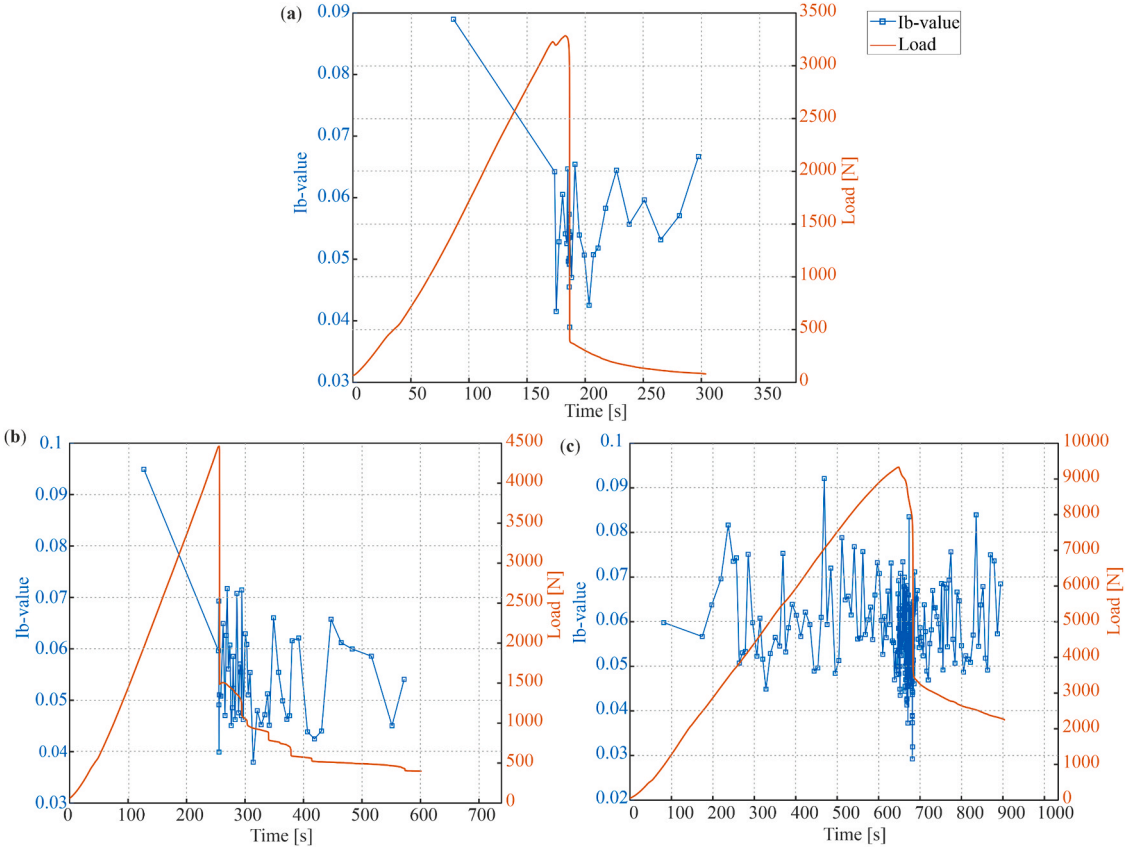

Fig. 9. Ib value characteristics profile together with load-time curve: (a) PC; (b) SFRC; and (c) SBRC.

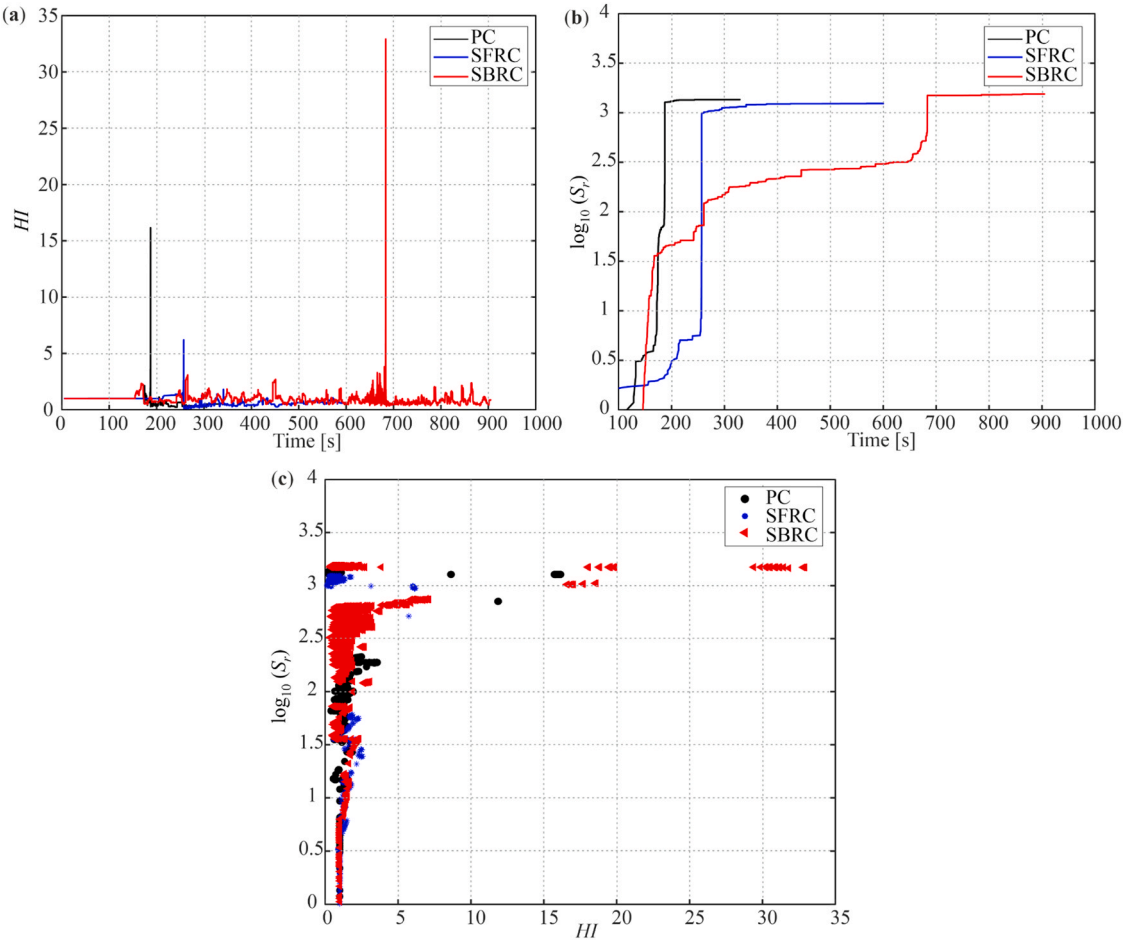

Fig. 10. AE intensity analysis of PC, SFRC and SBRC beams: (a) HI(t) vs. time; (b) log10 (Sr) vs. time; and (c) log10 (Sr) vs. HI(t).

matrix. However, a sharp peak in the HI(t) value was observed at 648 s, which caused brittle failure and was correlated with the development of macroscopic deformation. This abrupt increase in the HI(t) values indicated the splitting failure of the concrete beam, resulting in the release of high-energy hits.

In the case of the SFRC beam, it can be observed that it consistently exhibited lower HI(t) values during the bending process. It implies that the presence of the uniformly distributed steel fiber throughout the matrix significantly enhanced the steel-matrix interface. These stronger fibres and matrix matrices improved the post-cracking ductility, resulting in lower HI(t) values and behavior as compared to the SBRC beam. The occurrence of the main crack formation phase in the SFRC beam is indicated by the peak values observed in the HI(t) curve at 255 s. The peak values of HI(t) for both the SFRC and SBRC beams coincide with the observed progression of damage in the cumulative hits and cumulative energy diagram, indicating a correlation between the evolution of damage and the HI(t) values. The critical log10 (Sr) values of all tested beams as shown in Fig. 10b, revealed that the incorporation of steel fibres in concrete can lower the critical log10 (Sr) value of the specimen, while the presence of steel rebar can increase the critical log10 (Sr) value of the specimen. These higher and lower critical values of HI and log10 (Sr) can serve as indicators for determining the levels of deterioration in SFRC and SBRC beams regarding the selection of primary reinforcement. Moreover, the damage status of SFRC and SBRC beams can also be observed through the correlation between log10 (Sr) and HI(t) plots, as shown in Fig. 10c. In the case of the SBRC beam, the higher values of log10 (Sr) and HI(t) were observed located within the top right corner, which corresponds to a higher risk level and a larger safety reserve required for the specimen. Conversely, SFRC beam exhibited a lower intensity value which is located in the lower right corner. This phenomenon indicates that inclusion of SF to concrete limited the crack propagation size and produced less degree of damage to the concrete. Based on the above observations, it can be concluded that HI and log10 (Sr) values help us make the appropriate selection of primary reinforcement in concrete elements, which enhances the performance and lifespan of the structure and supports sustainability efforts.

3.2.6. Clustering of AE data

The K-Means algorithm is an iterative algorithm used for grouping the unlabelled N dataset into *k* clusters based on the nearest mean of each cluster. One of the important issues when using k-means clustering is estimating the best number of clusters. The Davies-

Bouldin (DB) index [48] and the Silhouette value [49] utilized the *k*-means algorithm for assessing the better clustering results on AE signals during the fracture process of reinforced materials. In this study, k values ranging from 2 to 10 were chosen for the PC, SFRC, and SBRC beams, with the mutation step size set at 1. Based on the k-values, the best number of clusters is selected and integrated with the k-means algorithm. The following AE parameters including count, duration, amplitude, and rise time, and count were selected for characterising the fracture features of tested beams. Fig. 11 displays the cluster evaluation results of the comparison between the Silhouette indices and Davies-Bouldin to choose the best number of clusters. According to the results, it can be observed that the optimum value of k is two for the SFRC and SBRC beams.

Fig. 12 shows two distinct clusters, one illustrating the progression of damage due to matrix cracking and the other representing the failure mechanism due to reinforcement/matrix debonding. These clusters were distinguished based on the correlation between peak amplitude vs. duration and the correlation between count vs. rise time to differentiate the failure mechanism. It can be observed that Cluster 1 consists mainly of low-amplitude signals, while Cluster 2 consists of higher-amplitude signals. Previous investigations have shown that high-amplitude AE signals are linked to fibre/matrix debonding, whereas AE signals with lower amplitudes are linked to matrix cracking [18]. It can be observed that the types of damage mechanisms observed in SFRC and SBRC beams. These were the matrix cracking failure, the failure mechanism involving the debonding of the steel fibres and the bar reinforcement from the matrix which were grouped into Cluster 1 and Cluster 2, respectively. Based on the peak AE amplitude characteristics, it can be concluded that the SBRC beam exhibited a higher microcracking activity with a longer duration than the SFRC beam. These higher activities are generated by splitting cracks at the weak interface. However, the combination of peak amplitude and duration is not sufficient to accurately distinguish the failure behaviour in SFRC and SBRC beams. Therefore, a relative distribution pattern of count versus rise time was introduced to further distinguish the failure mechanisms.

For the SBRC beam, a high number of 3056 AE signals with a rise time of 2.309×10^{4}[μs] was observed in Cluster 1, which are linked to matrix failure. This suggests that the SBRC beam experienced dominant matrix cracking during the initial loading, leading to the generation of higher microcracks and continuous damage development throughout the loading phase. In contrast, Cluster 1 of the SFRC beam showed a lower number of 275 AE signals with a shorter rise time of 0.236×10^{4}[μs]. This shows a different failure mechanism observed in SFRC beam where lower microcracks are merged due to stronger bridging effects at the fracture zone area, preventing the extent of crack propagation. Similarly, significant differences in AE counts were observed in Cluster 2. Cluster 2 of the SBRC beam emitted 14934 AE counts with a high-rise time of 10.41×10^{4}[μs], indicating failure mechanisms related to bar/matrix debonding. Cluster 2 of the SFRC beam exhibited 8704 AE counts with a shorter rise time of 4.127×10^{4}[μs], indicating failure mechanisms associated with steel fibre/matrix debonding. In summary, these findings indicate the SBRC beam experienced more microcracking activity due to the rapid development of splitting cracks, whereas the SFRC beam coalesced microcracks and reduced the degree of damage to concrete.

3.3. DIC observation

DIC data is used to provide insights into the analysis of surface displacements and deformations, allow the distribution of strain, and visualize how cracks initiate and develop within concrete [50]. This information is crucial for identifying potential areas of damage and understanding aspects of the evolution of structural responses under external loading. In this study, the progression of damage behaviour in normal concrete beam incorporated with steel fibres and bar reinforcement was analysed using DIC images taken during the bending test. The analysis was carried out in the specific area of interest (AOI) to analyse the crack propagation. The strain component images obtained at different load levels for the PC, SFRC, and SBRC beams in the horizontal and vertical direction are shown in Fig. 13 and Fig. 14, respectively. Three stages were selected to monitor the crack development phases and morphology of each specimen: the phase at 90% pre-peak, the peak phase, and the post-peak phase. The results show that, for the PC beam, single crack propagation can only be observed at the main crack stage (at the peak load), as shown in Fig. 13a. After attaining its peak value, this cracked zone penetrated to a depth of nearly 90% of the specimen size.

However, in the case of the SFRC beam, the first significant microcrack deformation was observed 20 mm from the centre of the beam during 90% of the pre-peak load. As the load increases, microcracks gradually propagate and macrocracks emerge and increase until they coalesce, causing main crack localization at the peak load. At the peak load stage, a prominent crack developed in the mid-

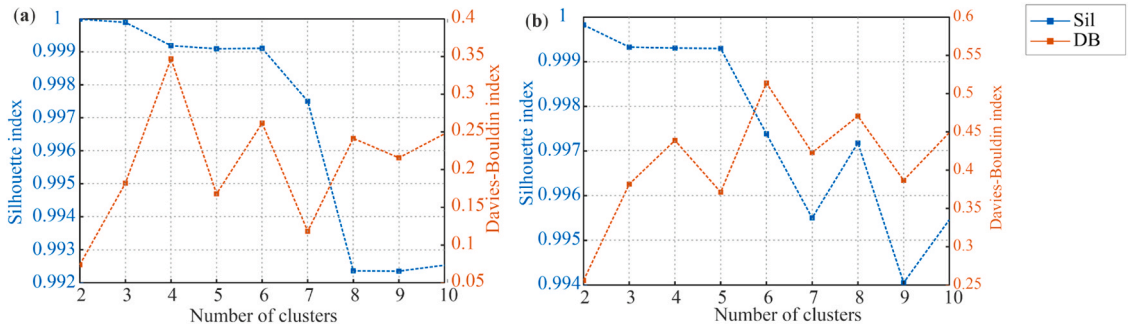

Fig. 11. The number of clusters evaluated by Davies–Bouldin index and Silhouette value: (a) SFRC; and (b) SBRC.

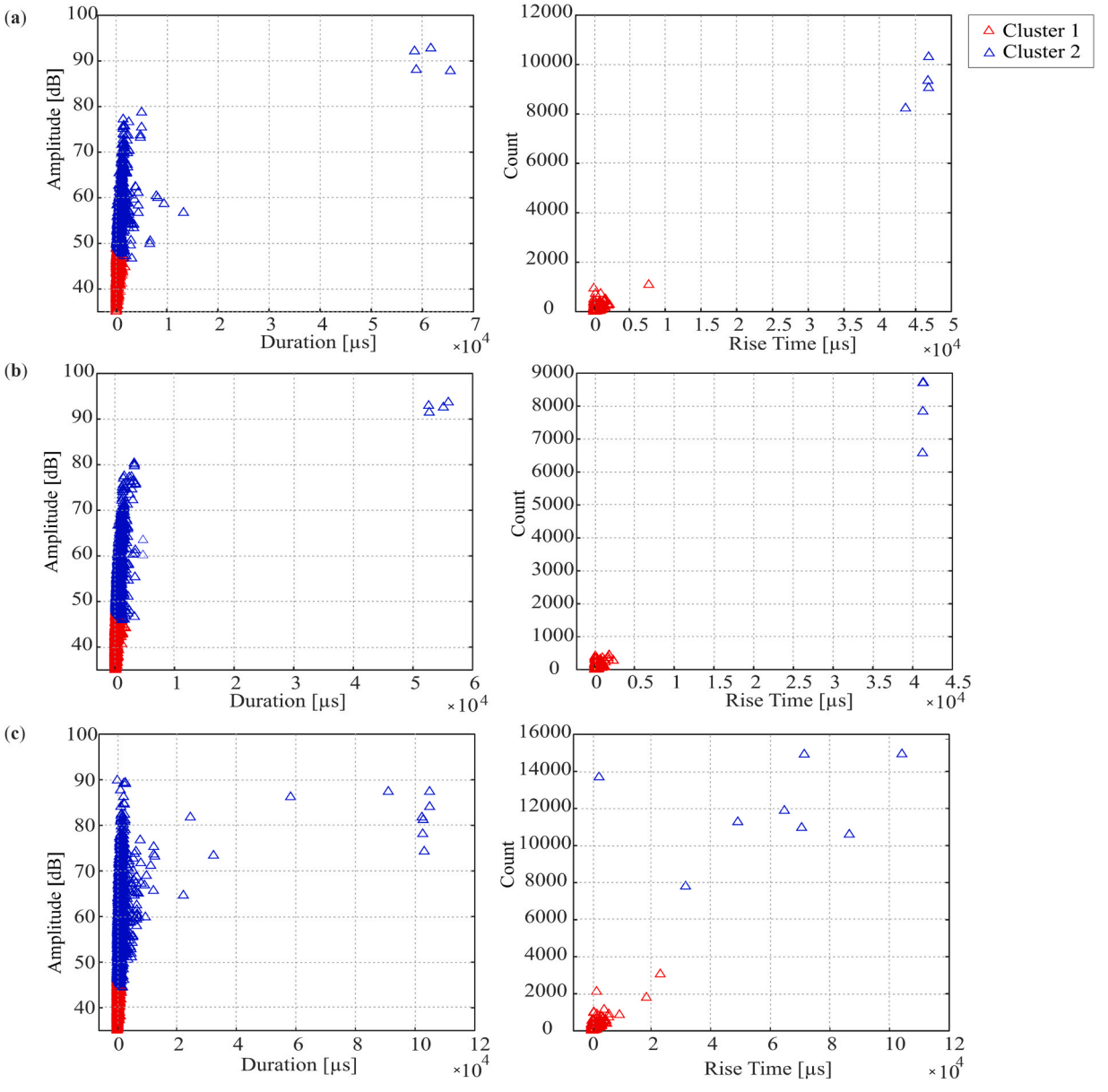

Fig. 12. Clusters distribution patterns by k-means algorithm of amplitude vs. duration and count vs. rise time: (a) PC; (b) SFRC; and (c) SBRC.

span of the beam and penetrated to a depth of approximately 40% of its height. This indicates that the crack-bridging capacity of steel fibres shrinkage the microcracks at the cracked surface area and redistributes the stresses evenly throughout the matrix. It prevents crack width propagation inside the matrix and increases the ductility of the material by enabling it to absorb higher energy through non-elastic deformations. After the peak phase, the crack width extended due to fibres entering the traction-free zone and did not make a significant contribution to the crack resistance, which resulted in a substantial loss of elastic stiffness. At this stage, the crack width exceeded approximately 0.05 mm and became visible to the human eye. For the SBRC beam, two prominent splitting cracks are initiated from the reinforced bar and propagated in the radial direction across the beam length at 90% of the pre-peak load. These splitting cracks covered 90% of the beam width area, more than that of the SFRC beam. At a peak value, the length of these splitting cracks remained constant and did not significantly enhance the ductility of the beam after the onset of cracking. This indicates that the fracture magnitude during the formation process of the primary crack in the SBRC beam is larger compared to the SFRC beam. After the peak period, the width of a diagonal crack increased and a high degree of splitting cracking was observed due to insufficient confinement and reinforcement spacing.

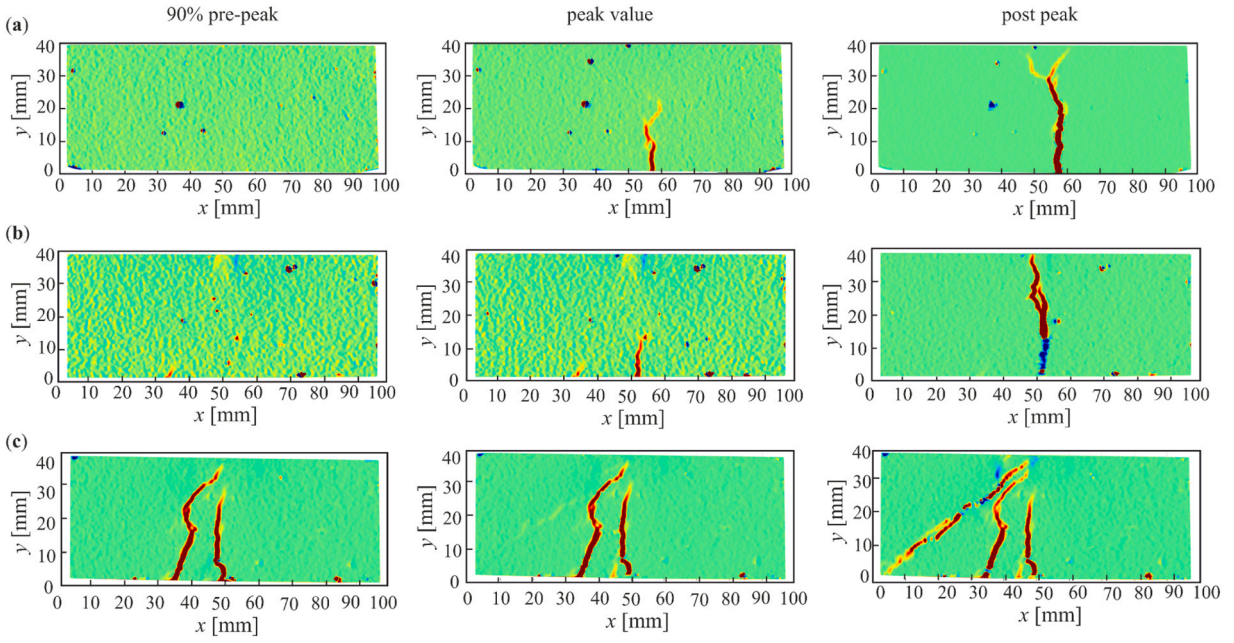

Fig. 13. DIC observation (strains ε_x) for fracture evolution at 90%pre-peak, peak, and post-peak loading stages: (a) PC; (b) SFRC; and (c) SBRC.

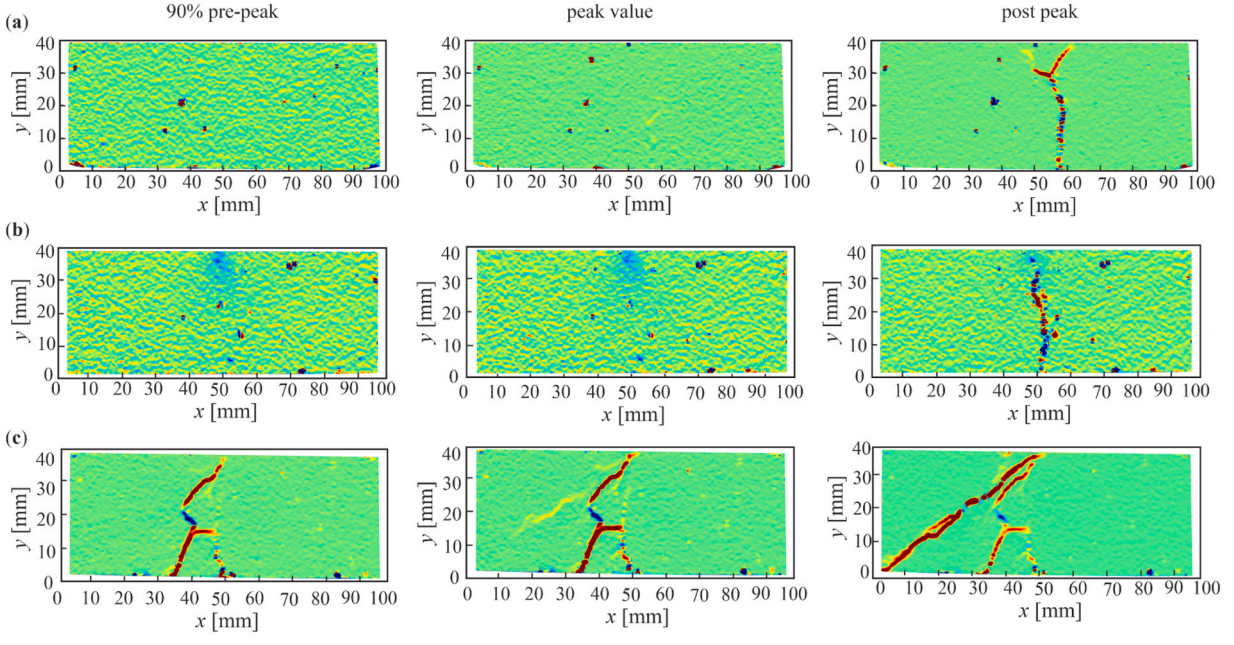

Fig. 14. DIC observation (strains ε_y) for fracture evolution at 90%pre-peak, peak, and post-peak loading stages: (a) PC; (b) SFRC; and (c) SBRC.

3.4. Integration of DIC images and local AE energy for fracture evolution

The integration of local AE energy and DIC data offers new insights for monitoring the fracture evolution of reinforced concrete elements. According to Bakour et al.[29], local AE energy is the fracture energy associated with microcrack events within the local fracture process zone (FPZ), which exhibits a strong correlation with the cumulative fracture energy. This combined approach provides a new quantitative feature, to monitor the evolution of the fracture process in concrete elements, enabling the advancement of construction materials and methodologies. When the specimen is fractured, the crack energy is released as an elastic waveform in terms of events and propagates from the crack location to the AE transducers at the specimen surface. AE sensors can detect this local AE energy

value and pinpoint the source of each event location by evaluating the AE wave's arrival time differences and AE wave speed in the materials. In this study, the speed of AE wave value calculated from the arrival time differences was 2000 m/s. The local AE energy as microcracking events were plotted in a two-dimensional format and correlated with DIC data. The hyperbolic diagrams are used to check the location of a certain AE event for two-dimensional planar positioning with the help of AE Vallen post-processing program

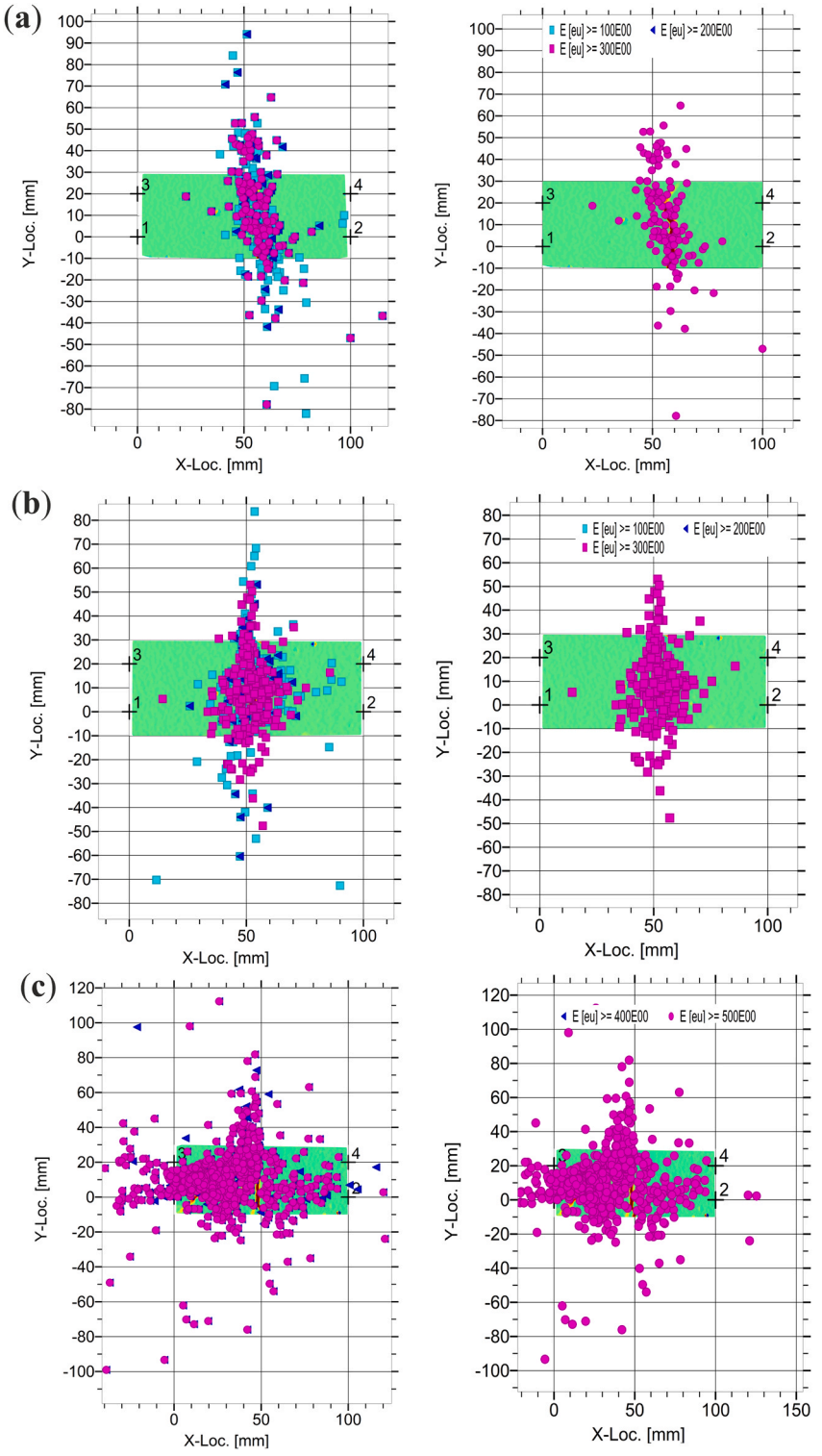

Fig. 15. 2D-localization maps of AE microcracking events by integrated local AE energies and DIC data: (a) PC; (b) SFRC; and (c) SBRC.

and the location analyser function [30,51].

The 2D source localization of AE events in terms of local AE energy integrated with the DIC results for PC, SFRC, and SBRC beams is presented in Fig. 15. These maps illustrate three different levels of microcracking AE events in terms of local fracture energy. It can be observed that the ordinary concrete beam exhibited fewer microcracking AE events within FPZ, which had lower local AE energy and was located away from the main crack localization path. This indicates that a larger fracture damage area was developed within FPZ, leading to a faster crack growth rate in the fracture process zone. Conversely, the uniformly distributed steel fibres generated higher localized AE energy events within the FPZ due to the cracked-bridging effect across cracked sections. This bridging effect enhances the ductility of SFRC beam, allowing them to withstand greater deformation before ultimate failure. When adding traditional reinforcement to concrete, a higher number of AE events was observed outside the FPZ as compared to SFRC beam. This was due to slippage of the bar reinforcement (lack of distributed reinforcement) and insufficient cover thickness, resulting in multiple splitting cracks along the length of the bar reinforcement. The presence of these multiple cracks is associated with increased macrocracking activity and SBRC beam did not significantly enhance the ductility of the beam after the onset of cracking.

4. Conclusions

This study investigated the fracture behaviour of SFRC and SBRC beams extracted from larger prisms subjected to three-point bending tests by employing two non-destructive monitoring techniques, acoustic emission (AE) and digital image correlation (DIC). The damage evolution with respect to crack formation and propagation were analyzed using various AE parameters. The unsupervised k-means clustering algorithm was used to distinguish between matrix failure and matrix/fibre-rebar debonding, offering valuable insights into structural health condition. DIC technology facilitated the visualization of crack propagation within the specific area of interest. Furthermore, the integration of localized AE fracture energy, indicative of microcrack events, with DIC data enabled the validation of damage source localization and surface crack characteristics analyzed by AE and DIC testing methods. The main conclusions are summarised as follows:

1. The parameter-based AE results demonstrated that during the pre-peak loading phase, a greater level of microcracking activity predominated in SBRC beams compared to SFRC beams. This intensified microcracking activity manifested as a steeper rise in the cumulative AE hits curve, accompanied by higher amplitude AE events.
2. The AE energy curve for SFRC beams showed an evident flat region following the main cracking stage, indicating pseudo-ductile behavior. This implies that SFRC beams exhibited a superior ability to arrest crack propagation and enabled the matrix to absorb more energy. Therefore, SFRC beams demonstrated an improved post-cracking softening behavior compared to SBRC beams.
3. A comparison of the Ib-value analysis revealed that SBRC beams had a lower Ib value (0.029) at the main cracking stage than the SFRC beams (0.039). Consequently, the SBRC beams experienced severe cracking, while the SFRC beams appeared to mitigate severe cracking resulting in a smaller fracture size than the SBRC beams.
4. The signal intensity analysis of HI and log10 S_r revealed that SBRC beams produced more macrocracks with stronger signal characteristics than SFRC beams. This observation is further supported by the correlation between HI(t) and log10 $S_r(t)$. For SBRC beams, higher values of both indices are clustered in the top right corner, signifying a higher risk level and a correspondingly larger safety reserve required for these beams.
5. The k-means clustering algorithm effectively distinguished between the distinct failure mechanisms in SFRC and SBRC beams, including matrix cracking and fiber-rebar/matrix debonding events.
6. The DIC images showed that SFRC beams generated a smaller crack width during the pre-peak and peak load phases than SBRC beams.
7. The integration of localized AE fracture energy, indicative of microcrack events, with DIC data indicated that the SBRC beams experienced concentrated AE event localizations outside the area of the fracture zone, resulting in a higher degree of microcracking activity than the SFRC beams.

The novelty of this study aimed to compare the fracture performance of SFRC and SBRC beams during the main cracking stage, regardless of their strength. Specifically, the study focused on understanding how the influence of these two types of reinforcement affects the ductility, post-cracking, and damage response of small-sized beam specimens cut from larger prisms. However, this research work is a preliminary stage and the analysis of the size effects needs to be further investigated in future work.

CRediT authorship contribution statement

Shahzad Ashraf: Writing – original draft, Visualization, Software, Methodology, Investigation, Formal analysis, Conceptualization. **Magdalena Rucka:** Writing – review & editing, Visualization, Supervision, Project administration, Methodology, Investigation, Funding acquisition, Formal analysis, Conceptualization.

Declaration of Competing Interest

The authors declare that they have no known competing financial interests or personal relationships that could have appeared to influence the work reported in this paper.

Data Availability

The raw data [52] required to reproduce these findings are available to download from https://doi.org/10.34808/j5a2-8s71

Acknowledgements

The study was supported by the National Science Centre, Poland, project no. 2019/35/B/ST8/01905.

References

[1] Y. Huang, J. Huang, W. Zhang, X. Liu, Experimental and numerical study of hooked-end steel fiber-reinforced concrete based on the meso- and macro-models, Compos. Struct. 309 (2023) 116750, https://doi.org/10.1016/j.compstruct.2023.116750.
[2] N. Makul, Modern sustainable cement and concrete composites: Review of current status, challenges and guidelines, Sustain. Mater. Technol. 25 (2020) e00155, https://doi.org/10.1016/j.susmat.2020.e00155.
[3] C. Zhang, H. Kordestani, M. Shadabfar, A combined review of vibration control strategies for high-speed trains and railway infrastructures: Challenges and solutions, J. Low. Freq. Noise Vib. Act. Control. 42 (2023) 272–291, https://doi.org/10.1177/14613484221128682.
[4] Y. Bu, M. Li, C. Wei, Z. Cheng, C. Cui, Y. Bao, Experimental and analytical studies on flexural behavior of composite bridge decks with orthotropic steel deck and ultra-high-performance concrete (UHPC) slab under negative moment, Eng. Struct. 274 (2023) 115190, https://doi.org/10.1016/j.engstruct.2022.115190.
[5] Y. Lin, J. Yan, Z. Wang, C. Zou, Theoretical models and reliability assessment of steel-UHPC-steel composite beams in offshore structures, Ocean Eng. 271 (2023) 113739, https://doi.org/10.1016/j.oceaneng.2023.113739.
[6] J.N. Almusawi, H. Hasan Muteb Aldaami, Push-out tests of a new prefabricated shear connector using normal and steel fiber reinforced concrete, Mater. Today Proc. 80 (2023) 1236–1242, https://doi.org/10.1016/j.matpr.2022.12.219.
[7] X. Zhang, J. Ou, Z. Wu, Effect of Circumferentially Nonuniform Lateral Tension on Bond Behavior between Plain Round Bars and Concrete: Analytical Study, J. Struct. Eng. 143 (2017), https://doi.org/10.1061/(asce)st.1943-541x.0001903.
[8] J. Saliba, D. Mezhoud, Monitoring of steel-concrete bond with the acoustic emission technique, Theor. Appl. Fract. Mech. 100 (2019) 416–425, https://doi.org/10.1016/j.tafmec.2019.01.034.
[9] J.M.J. Oliveira, C.S. Vieira, M.F.A. Silva, D.L.N.F. Amorim, Fracture modelling of steel fibre reinforced concrete structures by the lumped damage mechanics: Application in precast tunnel segments, Eng. Struct. 278 (2023), https://doi.org/10.1016/j.engstruct.2022.115487.
[10] V. Gribniak, A. Sokolov, Standardized RC beam tests for modeling the fiber bridging effect in SFRC, Constr. Build. Mater. 370 (2023) 130652, https://doi.org/10.1016/j.conbuildmat.2023.130652.
[11] A.B. Bhosale, S.S. Prakash, Crack Propagation Analysis of Synthetic vs. Steel vs. Hybrid Fibre-Reinforced Concrete Beams Using Digital Image Correlation Technique, Int. J. Concr. Struct. Mater. 14 (2020) 57, https://doi.org/10.1186/s40069-020-00427-8.
[12] S. Ashraf, S. Khan, V.K. Oad, Microcracking monitoring and damage detection of graphene nanoplatelets-cement composites based on acoustic emission technology, Case Stud. Constr. Mater. 18 (2023) e01844, https://doi.org/10.1016/j.cscm.2023.e01844.
[13] M. Rucka, E. Wojtczak, M. Knak, M. Kurpińska, Characterization of fracture process in polyolefin fibre-reinforced concrete using ultrasonic waves and digital image correlation, Constr. Build. Mater. 280 (2021) 122522, https://doi.org/10.1016/j.conbuildmat.2021.122522.
[14] A. Gallego, A. Benavent-Climent, E. Suarez, Concrete-Galvanized Steel Pull-Out Bond Assessed by Acoustic Emission, J. Mater. Civ. Eng. 28 (2016) 1–8, https://doi.org/10.1061/(asce)mt.1943-5533.0001372.
[15] A.A. Abouhussien, A.A.A. Hassan, Acoustic emission monitoring for bond integrity evaluation of reinforced concrete under pull-out tests, Adv. Struct. Eng. 20 (2017) 1390–1405, https://doi.org/10.1177/1369433216678864.
[16] E. Tsangouri, D.G. Aggelis, A review of acoustic emission as indicator of reinforcement effectiveness in concrete and cementitious composites, Constr. Build. Mater. 224 (2019) 198–205, https://doi.org/10.1016/j.conbuildmat.2019.07.042.
[17] M. Chai, X. Hou, Z. Zhang, Q. Duan, Identification and prediction of fatigue crack growth under different stress ratios using acoustic emission data, Int. J. Fatigue 160 (2022) 106860, https://doi.org/10.1016/j.ijfatigue.2022.106860.
[18] S. Tayfur, N. Alver, S. Abdi, S. Saatcı, A. Ghiami, Characterization of concrete matrix/steel fiber de-bonding in an SFRC beam: Principal component analysis and k-mean algorithm for clustering AE data, Eng. Fract. Mech. 194 (2018) 73–85, https://doi.org/10.1016/j.engfracmech.2018.03.007.
[19] A. Thirumalaiselvi, S. Sasmal, Pattern recognition enabled acoustic emission signatures for crack characterization during damage progression in large concrete structures, Appl. Acoust. 175 (2021) 107797, https://doi.org/10.1016/j.apacoust.2020.107797.
[20] L. Calabrese, G. Campanella, E. Proverbio, Noise removal by cluster analysis after long time AE corrosion monitoring of steel reinforcement in concrete, Constr. Build. Mater. 34 (2012) 362–371, https://doi.org/10.1016/j.conbuildmat.2012.02.046.
[21] I. Saha, R. Vidya Sagar, Classification of the acoustic emissions generated during the tensile fracture process in steel fibre reinforced concrete using a waveform-based clustering method, Constr. Build. Mater. 294 (2021) 123541, https://doi.org/10.1016/j.conbuildmat.2021.123541.
[22] A. Farhidzadeh, S. Salamone, P. Singla, A probabilistic approach for damage identification and crack mode classification in reinforced concrete structures, J. Intell. Mater. Syst. Struct. 24 (2013) 1722–1735, https://doi.org/10.1177/1045389X13484101.
[23] A. Behnia, H.K. Chai, T. Shiotani, Advanced structural health monitoring of concrete structures with the aid of acoustic emission, Constr. Build. Mater. 65 (2014) 282–302, https://doi.org/10.1016/j.conbuildmat.2014.04.103.
[24] O. Avci, O. Abdeljaber, S. Kiranyaz, M. Hussein, M. Gabbouj, D.J. Inman, A Review of Vibration-Based Damage Detection in Civil Structures: From Traditional Methods to Machine Learning and Deep Learning Applications, Mech. Syst. Signal Process. 147 (2020) 107077, https://doi.org/10.1016/j.ymssp.2020.107077.
[25] P. Mirgal, J. Pal, S. Banerjee, Online acoustic emission source localization in concrete structures using iterative and evolutionary algorithms, Ultrasonics 108 (2020) 106211, https://doi.org/10.1016/j.ultras.2020.106211.
[26] P. Mirgal, S. Banerjee, R. Singh, Acoustic and Fracture Energy Correlation in Mode I Fracture with Concrete Damage Plasticity Model and Three-Point Bend Experiment, J. Mater. Civ. Eng. 35 (2023), https://doi.org/10.1061/(ASCE)MT.1943-5533.0004673.
[27] J. Bu, X. Wu, H. Xu, X. Chen, The rate effect on fracture mechanics of dam concrete based on DIC and AE techniques, J. Strain Anal. Eng. Des. 57 (2022) 496–510, https://doi.org/10.1177/03093247211038131.
[28] M. De Smedt, E. Vandecruys, R. Vrijdaghs, E. Verstrynge, L. Vandewalle, Acoustic emission-based damage analysis of steel fibre reinforced concrete in progressive cyclic uniaxial tension tests, Constr. Build. Mater. 321 (2022) 126254, https://doi.org/10.1016/j.conbuildmat.2021.126254.
[29] A. Bakour, M.Ben Ftima, A. Chéruel, Combination of acoustic emission and digital image correlation monitoring for wedge splitting tests on large concrete specimens, Constr. Build. Mater. 322 (2022), https://doi.org/10.1016/j.conbuildmat.2022.126496.
[30] A. Boniface, J. Saliba, Z.M. Sbartaï, N. Ranaivomanana, J.P. Balayssac, Evaluation of the acoustic emission 3D localisation accuracy for the mechanical damage monitoring in concrete, Eng. Fract. Mech. 223 (2020), https://doi.org/10.1016/j.engfracmech.2019.106742.
[31] A. Okeil, K. Matsumoto, K. Nagai, Investigation on local bond behavior in concrete and cement paste around a deformed bar by using DIC technique, Cem. Concr. Compos. 109 (2020) 103540, https://doi.org/10.1016/j.cemconcomp.2020.103540.
[32] G. Xing, Y. Xu, J. Huang, Y. Lu, P. Miao, P. Chindasiriphan, P. Jongvivatsakul, K. Ma, Research on the mechanical properties of steel fibers reinforced carbon nanotubes concrete, Constr. Build. Mater. 392 (2023) 131880, https://doi.org/10.1016/j.conbuildmat.2023.131880.
[33] G. Lacidogna, G. Piana, F. Accornero, A. Carpinteri, Multi-technique damage monitoring of concrete beams: Acoustic Emission, Digital Image Correlation, Dynamic Identification, Constr. Build. Mater. 242 (2020) 118114, https://doi.org/10.1016/j.conbuildmat.2020.118114.

[34] T. Shiotani, Application of the AE improved b-value to quantiative evaluation of fracture process in concrete-materials, J. Acoust. Emiss. 19 (2001) 118–133.
[35] D.G. Aggelis, D.V. Soulioti, N. Sapouridis, N.M. Barkoula, A.S. Paipetis, T.E. Matikas, Acoustic emission characterization of steel fibre reinforced concrete during bending, in: Nondestruct. Charact. Compos. Mater. Aerosp. Eng. Civ. Infrastructure, Homel. Secur., 2010, SPIE, 2010 764912, https://doi.org/10.1117/12.847396.
[36] P.R. Prem, M. Verma, P.S. Ambily, Damage characterization of reinforced concrete beams under different failure modes using acoustic emission, Structures 30 (2021) 174–187, https://doi.org/10.1016/j.istruc.2021.01.007.
[37] A. Nair, C.S. Cai, Acoustic emission monitoring of bridges: Review and case studies, Eng. Struct. 32 (2010) 1704–1714, https://doi.org/10.1016/j.engstruct.2010.02.020.
[38] D.J. Hand, W.J. Krzanowski, Optimising k -means clustering results with standard software packages, 49 (2005) 969–973. ⟨https://doi.org/10.1016/j.csda.2004.06.017⟩.
[39] J. Xu, S. Ashraf, S. khan, X. Chen, A. Akbar, F. Farooq, Micro-cracking pattern recognition of hybrid CNTs/GNPs cement pastes under three-point bending loading using acoustic emission technique, J. Build. Eng. 42 (2021), https://doi.org/10.1016/j.jobe.2021.102816.
[40] H. Li, S. Meng, D. Shi, Q. Wei, Z. Xu, W. Zhao, Influence of moisture on ultrasonic propagation, acoustic emission activity, and failure mechanism in concrete media, Constr. Build. Mater. 386 (2023) 131499, https://doi.org/10.1016/j.conbuildmat.2023.131499.
[41] M. Liu, J. Lu, P. Ming, J. Song, AE-based damage identification of concrete structures under monotonic and fatigue loading, Constr. Build. Mater. 377 (2023) 131112, https://doi.org/10.1016/j.conbuildmat.2023.131112.
[42] R. Vidya Sagar, I. Saha, Application of acoustic emission testing in order to understand mode I fracture process in steel fibre reinforced concrete R. Vidya Sagar 1 *, Indrashish Saha 1 1, in: 15th Int. Conf. Fract., 2023.
[43] A. Carpinteri, G. Lacidogna, N. Pugno, Structural damage diagnosis and life-time assessment by acoustic emission monitoring, Eng. Fract. Mech. 74 (2007) 273–289, https://doi.org/10.1016/j.engfracmech.2006.01.036.
[44] G. Lacidogna, F. Accornero, A. Carpinteri, Influence of snap-back instabilities on Acoustic Emission damage monitoring, Eng. Fract. Mech. 210 (2019) 3–12, https://doi.org/10.1016/j.engfracmech.2018.06.042.
[45] E. Verstrynge, G. Lacidogna, F. Accornero, A. Tomor, A review on acoustic emission monitoring for damage detection in masonry structures, Constr. Build. Mater. 268 (2021) 121089, https://doi.org/10.1016/j.conbuildmat.2020.121089.
[46] S. Ashraf, M. Rucka, Microcrack monitoring and fracture evolution of polyolefin and steel fibre concrete beams using integrated acoustic emission and digital image correlation techniques, Constr. Build. Mater. 395 (2023) 132306, https://doi.org/10.1016/j.conbuildmat.2023.132306.
[47] D. Jung, W.R. Yu, W. Na, Use of acoustic emission b(Ib)-values to quantify damage in composites, Compos. Commun. 22 (2020), https://doi.org/10.1016/j.coco.2020.100499.
[48] F. Informa, W.R. Number, M. House, M. Street, J.C. Dunn, Well-Sep. Clust. Optim. Fuzzy Partit. Well-Sep. Clust. Optim. Fuzzy Partit. (2008) 37–41.
[49] P.J. Rousseeuw, Silhouettes: A graphical aid to the interpretation and validation of cluster analysis, J. Comput. Appl. Math. 20 (1987) 53–65, https://doi.org/10.1016/0377-0427(87)90125-7.
[50] N. Gehri, J. Mata-Falcón, W. Kaufmann, Automated crack detection and measurement based on digital image correlation, Constr. Build. Mater. 256 (2020) 119383, https://doi.org/10.1016/j.conbuildmat.2020.119383.
[51] W. Zhou, Z. Lv, Z. Li, X. Song, Acoustic emission response and micro-deformation behavior for compressive buckling failure of multi-delaminated composites, J. Strain Anal. Eng. Des. 51 (2016) 397–407, https://doi.org/10.1177/0309324716645244.
[52] M. Rucka, S. Ashraf, *Acoustic emission signals in concrete beams under 3-point bending (plain concrete, steel fibre*, in: *reinforced concrete, steel bar reinforced concrete)* [dataset], Gdańsk University of Technology, 2024, https://doi.org/10.34808/j5a2-8s71.